TiO_2 nanorods-based photoelectrodes for dye solar cells with tunable morphological features

Michele Manca,[1] Luisa De Marco,[1] Roberto Giannuzzi,[1] Rita Agosta,[1] Charu Dwivedi,[4] Antonio Qualtieri,[1] Viresh Dutta[4] and Giuseppe Gigli[1,2,3]

[1] Center for Bio-Molecular Nanotechnology of IIT - Fondazione Istituto Italiano di Tecnologia, Via Barsanti, 73010, Arnesano (Lecce), ITALY

[2] National Nanotechnology Laboratory of CNR - Istituto Nanoscienze, Distretto Tecnologico Via Arnesano 16, 73100 Lecce, ITALY

[3] Dipartimento di Matematica e Fisica "E. De Giorgi", Universita' del Salento, Via Arnesano, 73100 Lecce, ITALY

[4] Indian Institute of Technology, Center for Energy Studies, Hauz Khas, New Delhi-110016, INDIA

CORRESPONDING AUTHOR E-MAIL: michele.manca@iit.it – tel. +39 0832 1816238

KEYWORDS: TiO_2 nanorods, photoelectrodes, electrochemical impedance spectroscopy

ABSTRACT

The ability to create photoanodes in which the structural and morphological features of the underlying TiO_2 nanocrystalline constituents provide a tailored nanotexture with a higher degree of functionality still represents an indispensible step toward boosting the ultimate light-to electricity conversion of photoelectrochemical devices. This is especially evident for dye solar cells. In this paper we have systematically analyzed the impact of several different TiO_2 nanorods morphologies on the most meaningful electrochemical features of the mesoporous photoelectrode of a dye solar cell. The most relevant findings have been then adopted as design criteria to realize an optimized multilayered photoelectrode with a properly engineered architecture which embodies three different breeds of nanocrystal with synergistic peculiarities. It exhibited superior power conversion efficiencies with respect to conventional nanoparticles-based reference film.

INTRODUCTION

The performance of solar energy conversion devices employing mesoscopic photoelectrodes depends critically on their nanostructure. This is evident for a dye solar cell (DSC), where every single step of the energy conversion process is characterized by its own reaction rate constant [1]. Charges separation

in a DSC is driven by kinetic mechanisms; the most critical parameter is associated to the electrons transport in the TiO_2 mesoporous photoelectrode, which is the key component of a DSC, since the majority of the photoinduced energy conversion steps take place either in the bulk phase of the underlying semiconductor network or on its surface.

For an efficient working mechanism, a large surface area at the dye/TiO2 semiconductor interface is necessary to achieve extended chemisorption of dye molecules, whereas a porous structure is required to improve the interaction of the electrolyte with the oxidized dye to induce an efficient regeneration of the dye. Actually, a film consisting of 15-nm nanoparticles with a thickness of 10 μm has been demonstrated to have an internal surface area as high as 780 cm^2 for each 1 cm^2 of geometric surface [2]. Moreover, TiO_2 mesoporous films have to be characterized by good adhesion to the conductive glass and absence of cracks as well as by the presence of good interconnections between nanosized titania nanoparticles. This avoids charge-carrier accumulation, allows for efficient electron flow, and, finally, assures current collection at the back contact of the photoelectrode [3]. Nevertheless, nanoparticle films are not thought to offer an ideal structure suitable to electron transport. A major source of non-ideality stands within the fact that electron transport undergoes trapping and detrapping phenomena, i.e., the injected electrons can be captured by trap states and, however, be again thermally emitted back to the conduction band. [4,5] Hence it can be conveniently described with a trap-limited diffusion model. A density of trap states that increases exponentially towards the conduction band edge is found in these nanoporous electrodes.

Employing one-dimensional nanostructures in DSCs is an attempt to figure out this problem based on a consideration that the one-dimensional nanostructures such as nanowires, nanorods and nanotubes can provide direct pathways for electron transport from the site occurring electron injection to the conducting film of collector electrode. As such, it is expected to get electron transport faster than in nanocrystalline film. This has been evidenced by experiments which reveal that the electron transport in photoelectrode comprised of single crystal nanowires is even 100 times faster than that in the case of nanocrystalline film [6]. A fast electron transport may lower the opportunity of photogenerated electrons to react with the positive species in the electrolyte and, therefore, significantly suppress the interfacial charge recombination [7,8].

To date the highest power conversion efficiencies have been achieved with photoanodes consisting of a dye adsorption layer (20 nm sized TiO2 nanoparticle) and light scattering layer (400 nm sized particle) [9]. The small nanoparticles have larger surface areas to adsorb dye molecules but present inefficient light scattering ability and hence result in poor light-harvesting efficiency. On the other

hand, large particles with flat surfaces possess excellent light scattering properties but are not suitable as photoanode materials because of less dye loading capability.

In addition, in order to obtain fast electron diffusion rates and long electron lifetimes, anisotropically shaped TiO2 nanostructures were implemented, such as all-linear [10-14] or branched nanorods, [15-17] nanowires [18,19] and nanotubes arrays. [20,21] However, modest PCE values have been reported to date, mainly because of the reduced internal surface area offered by photoanodes which employ nanorods or nanowires with a mean size larger than 100 nm [12,22,23] and/or the severe degradation of the original structural–morphological features of the selected anisotropic TiO2 nanocrystals upon sintering.[11,15,16]

Hence, the real challenge is to design and fabricate a nanostructured photoanode which simultaneously has a large surface area to absorb more dye molecules, efficient light scattering ability and fast electron transport (as represented in the sketch shown in Figure 1).

Starting from these remarks, we here report some of the recent experimental efforts which have been put by our research group into the development of highly efficient photoelectrodes for DSCs which embodies different families of shape-tailored TiO_2 nanocrystals in such a way to advantageously exploit their topological features within an optimized multistacks photoelectrode.

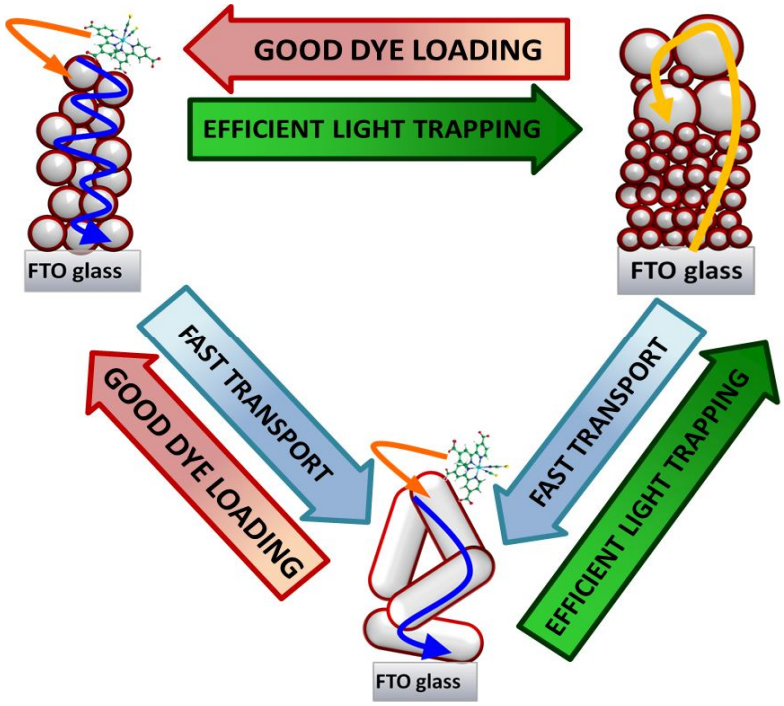

Figure 1. Schematic representation of the main issues - often complementary - which should be addressed by an efficient photoelectrode

EXPERIMENTAL DETAILS

Three families of alkyl-carboxylate-capped anatase TiO2 linear nanorods (NRs) with a variable aspect ratio (AR), henceforth referred to as sample ‘‘AR4-NRs’’, ‘‘AR8-NRs’’, and ‘‘AR16-NRs’’, respectively, were synthesized as follows:

Synthesis of AR4 and AR8 NRs: were obtained by low-temperature trimethylamine N-oxide catalyzed hydrolysis of titanium isopropoxide (TTIP) in nonanoic acid [22] and oleic acid, [23] respectively.

In a typical synthesis, 15 mmol of TTIP were dissolved in 70 g of degassed nonanoic acid or oleic acid and the resulting solution was then reacted with 5 mL of an aqueous 2 M trimethylamine N-oxide solution at 100° C for 96 h.

Synthesis of AR16-NRs: were obtained by high-temperature nonhydrolytic condensation of TTIP with oleic acid.[24] In a typical synthesis TTIP (17.7 mL, 60 mmol) was added to 50 g of oleic acid at room temperature. Then, the resulting mixture was gradually heated to 270°C at a rate of about 10°C min^{-1} and then kept at this temperature for 2 h.

Synthesis of branched NRs:

Two families of alkyl-carboxylate-capped anatase branched TiO2 nanostructures, namely sheaf-like branched nanorods, henceforth referred to as sample ‘‘B-NRs’’, and thereof derived braid-like nanorod bundles, labelled as ‘‘BB-NRs’’, were synthesized by aminolytic decomposition of titanium oleate complexes at high temperatures [17];

as a general procedure, 3 g of 1-octadecene, 3 mmol of oleyl amine and 11 mmol of oleic acid were loaded in a three-neck flask and degassed at 120°C for 45 min, after which the mixture is cooled down to 50°C under N_2 flow. At this point, 1 mmol of titanium tetrachloride ($TiCl_4$) dissolved in 1 ml of 1-octadecene was added and the flask was heated up to 290°C at a ramp rate of 25°C/min. After heating for 1 h at 290°C, the reaction could be either stopped to collect B-NRs or continued by performing alternated additions of a 0.5 M oleic acid /1-octadecene solution (injected in single portion) and of a 0.5 M $TiCl_4$/1-octadecene solution (delivered at a constant rate of 0.1 mL/min by means of a syringe pump). The BB-NRs were obtained upon adding an extra 16 mmol of $TiCl_4$ after the primary injection. After the synthesis, the TiO_2 nanocrystals were precipitated upon addition of ethanol or 2-propanol:acetone mixtures, separated by centrifugation, and then washed with acetone to remove the excess surfactant residuals. Then, the resulting products were easily redispersed in an apolar organic solvent, such as toluene or chloroform.

TiO_2 paste preparation and DSSC fabrication: nanocrystal suspensions (containing 4% wt/wt of TiO_2 as revealed by ICP-AES analysis) were stirred at 60°C for 6 h with ethylcellulose previously dissolved in toluene (10% wt/wt). Then, the solvent exchange was carried out as follows: terpineol was added

and the resulting mixture was stirred again for 1 h; finally toluene was removed by a rotary evaporator to obtain pastes suitable for doctor-blade deposition. The paste had the following weight percentage composition: TiO_2: 12%; organic capping residuals: 15%; ethylcellulose: 5%; terpineol: 68%. The TiO_2 paste was deposited onto F-doped tin oxide conducting glass (15 ohm/sq., provided by Solaronix S.A.). by doctor blading and dried at 160°C for 15 minutes. This procedure was repeated several times in order to obtain the desired film thickness, followed by sintering at 480°C for 30 min. For comparison, conventional nanocrystals-based photoanodes were prepared by deposition of commercial colloidal pastes.

After cooling to 80 °C, the TiO_2 electrodes were immersed into a solution 0.2 mM of N719 (provided by Solaronix S.A.) in a mixture of acetonitrile and tert-butyl alcohol (v/v, 1:1), and kept at room temperature for 14 h. The solar cells were assembled by placing a platinum-coated conducting glass (counter electrode) on photoelectrode and sealed with a 50 μm thick Surlyn hot-melt gasket. The redox electrolyte (0.1M LiI, 0.05M I_2, 0.6M 1, 2-dimethyl-3-propylimidazolium iodide, and 0.5M tert-butylpyridine in dried acetonitrile) was introduced into the inter-electrode void space through a hole pre-drilled on the back of the counter electrode.

Nanocrystals and devices characterization: Low-magnification transmission electron microscopy (TEM) images of TiO_2 nanocrystals were recorded with a Jeol Jem 1011 microscope operating at an accelerating voltage of 100 kV. The thickness and the active area dimensions of the films were measured with Tencor Alpha-Step 500 Surface Profiler. A Varian Cary 5000 UV–Vis Spectrophotometer was used to measure the diffuse reflectance spectra of the as-prepared films. Scanning electron microscopy (SEM) characterization of TiO_2 photoelectrode morphology was performed with a RAITH 150 EBL instrument. Photocurrent-voltage I-V measurements were performed using a Keithley unit (Model 2400 Source Meter). A Newport AM 1.5 Solar Simulator (Model 91160A equipped with a 300W Xenon Arc Lamp) serving as a light source. The light intensity (or radiant power) was calibrated to 100 mW cm^{-2} using as reference a Si solar cell. Electrochemical impedance spectroscopy (EIS) was performed by an AUTOLAB PGSTAT 302N (Eco Chemie B.V.) in a frequency range between 300 kHz–30 mHz. The impedance measurements were carried out at different voltage biases in the dark. The resulting impedance spectra were fitted with ZView software (Scribner Associate).

RESULTS AND DISCUSSION

Linear nanorods of TiO_2 with variable aspect ratio (4, 8 and 16, respectively) and relatively bulkier branched nanostructures (in the form of open-framework sheaf-like nanorods and more compact braid-like nanorod bundles, respectively) were effectively employed to fabricate five series of mesoporous film photoelectrodes.

The major challenge was to preserve the original morphologies of the nanocrystals: rod shape and small dimension might be considered the most important parameters because they have a tremendous effect on transport properties and light harvesting. It has been revealed that removal of the capping layer by washing (with ethanol or isopropyl alcohol) or drying procedure is very problematic and mostly inconvenient due to the inducement of serious coalescence phenomena. We observed, in fact, that, when dried or spray-dried (fig 2a), nanocrystals lose their original morphology and form micrometersized aggregates that are no more separable by conventional milling techniques. Such aggregation phenomena have the effect of reducing the surface area (fig 2b), thus the light-harvesting capability of the photoelectrode, as well as to induce the formation of cracks during the sintering process as observable in Figure 2.

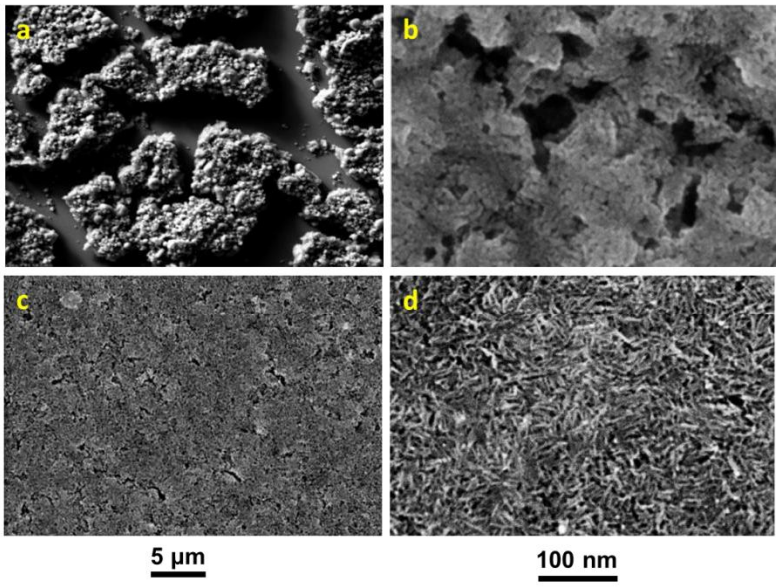

Figure 2. SEM images of NRs-based electrodes obtained after removal (a, b) and through the presence (c, d) of the original organic capping layer

What we did was instead to use the reaction product without completely removing the residual organic compounds. After the supernatant was eliminated by centrifugation, the precipitate was directly mixed with proper polymeric binders. The hydrophobic oleate surfactant shell employed in the synthesis

plays a pivotal role in maintaining good nanoparticle dispersion even during the post-synthesis process steps. It in fact guarantees the kinetic stabilization against undesired irreversible coalescence phenomena and ensures retention of the size/shape features and acts as a "soft template" that keeps the nanoparticles well-separated. It is hence fundamental for the formation of an high quality mesoporous network during the sintering process. (fig 2 c,d) [1,13]

Fig. 3 illustrates TEM (I-V) and SEM (a-l) overview images of the AR4-NR-, AR8-NR-, AR16-NR-, B-NR-, and BB-NR-based photoelectrodes, respectively, obtained after the sintering cycle (maximum temperature of 480°C). The TiO_2 mesoporous films were characterized by excellent adhesion to the conductive glass, good homogeneity and the absence of aggregates and cracks. In all cases the elongated nanocrystal morphology appeared to have been adequately preserved and the mean size of the constitutive elements of the photoelectrodes was coherent with the dimensions of the original nanocrystals, and no coarsened nanostructures were observed.

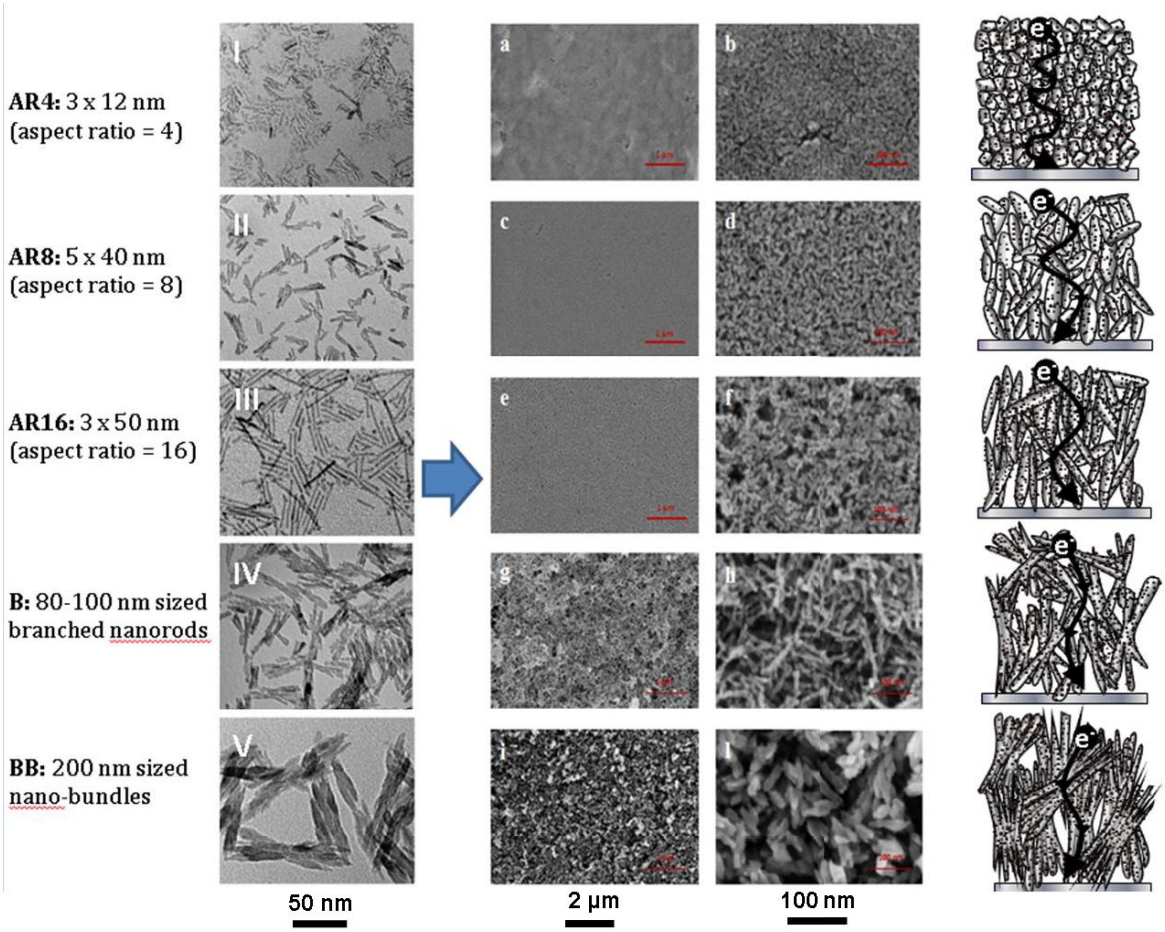

Figure 3. TEM (I-V) and SEM images at different magnification of the sintered photoelectrodes prepared from AR4-NRs (a and b), AR8-NRs (c and d), AR16-NRs (e and f), B-NRs (g and h) and BB-NRs (i and l), along with corresponding sketches highlighting their nano-/microstructure.

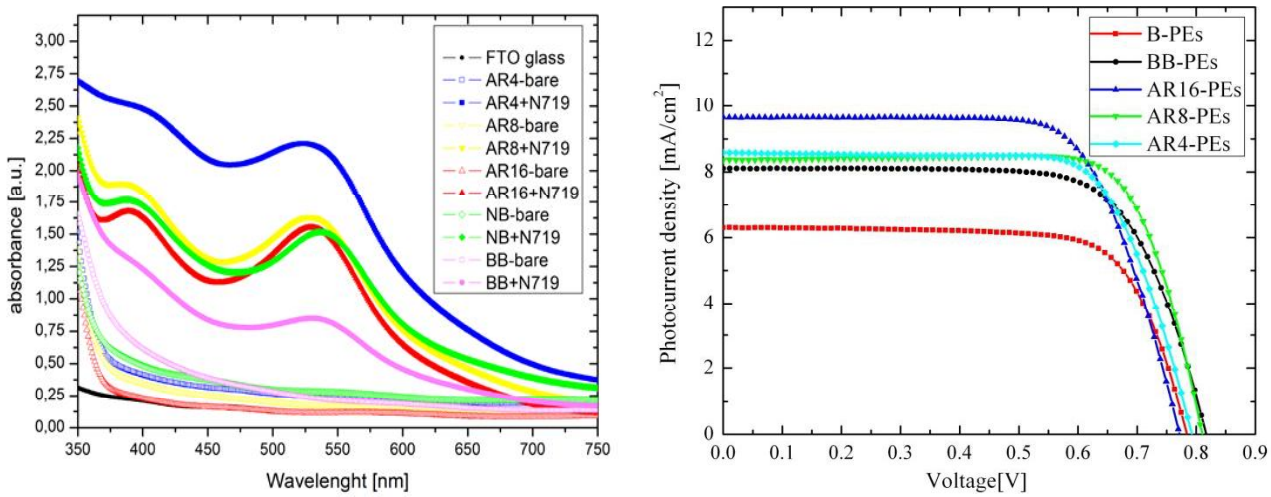

Figure 4. a) UV-VIS absorption spectra of 6 um thick NRs-based PEs before and after the dye up-taking process. b) IV curves of DSCs implementing the same PEs measured under 1 sun illumination

Photovoltaic numbers measured under 1 sun illumination for DSCs implementing 6 um thick photoelectrodes are reported in Table 1 beside to the amount dye molecules up-taken by each photoelectrode.

Table 1 Dye loading capability and photovoltaic performance parameters of DSSCs implementing 6 µm thick NRs-based photoelectrodes. PV Characteristics recorded on sensitized 0.28 cm2 electrodes

Photoelectrode	Dye Loading [mol*cm^{-2}]	η [%]	FF	V_{OC} [V]	J_{sc} [mA/cm^2]
B-PEs	$1.6*10^{-7}$	**3.89**	0.73	0.78	6.80
BB-PEs	$1.1*10^{-7}$	**4.68**	0.71	0.82	8.10
AR16-PEs	$1.7*10^{-7}$	**5.24**	0.70	0.77	9.65
AR8-PEs	$2.0*10^{-7}$	**5.20**	0.77	0.81	8.36
AR4-PEs	$2.6*10^{-7}$	**4.92**	0.72	0.79	8.59

The first issue to be highlighted is the trend in the photocurrent density associated to linear NRs with increasing aspect ratio: it was just opposite to the trend featuring their dye-adsorbing capabilities. This means that inherent electron transport properties of the films overwhelmed the impact of the surface area and hence of the dye-loading capability (which is also reported in Table 1) on the ultimate photocurrent values: AR16-NRs based films produced indeed the highest photocurrent density (9.65 mA cm^{-2}) despite their relatively lower surface area.

Secondly, PEs made from sheaf-like B-NRs exhibited a dramatically lower photocurrent density (6.80 mA cm^{-2}) with respect to AR16-NRs, despite the fact that they were featured by comparable specific surface area. Moreover, PEs consisting of large bundle-like BB-NRs presented a surprisingly high photocurrent density (8.10 mA cm^{-2}) when taking into account their reduced amount of adsorbed dye molecules. They also provided the highest V_{OC} value (0.82 V) which can be presumably explained as being due to the reduced number of nanocrystal interconnections and hence, of charge-recombination sites.

Electrochemical impedance spectra (EIS) were measured at different bias potentials and analyzed through the well-known equivalent circuit based on the transmission line model. [25]

Both the charge transfer resistance Rct and the transport resistance Rt were extrapolated from the Nyquist plots measured in dark condition. R_{CT} shows an exponential dependence on the bias voltage, which can be satisfactorily described by the expression: [25, 26]

—— [3]

where β is the transfer coefficient, which was calculated according to the model proposed by Bisquert et al.[27] A reaction order (β), typically in the range of 0.5-0.7, is used to provide an empirical description of sublinear recombination kinetics [27] which takes into account the fact that electrons may be transferred from occupied levels located in the energy gap.[27,28] A value of $\beta \approx 0.5$ was extrapolated for all the families of photoelectrodes, which indicated that no noticeable differences in the recombination's reaction order were associable with nanocrystals featured by any particular morphology.

The logarithmic trend of R_{CT} as a function of the corrected bias voltage is reported in Figure 5a. A huge enhancement of R_{CT} was observed for BB-NRs-based photoelectrodes with respect to cells built with other nanocrystal shapes, and in particular with respect to B-NRs.

The electron diffusion resistance, R_T, shown in Figure 5b, decreased exponentially with the corrected voltage. Since the R_T is inversely proportional to the density of electrons at the transport level, it is generally expressed in terms of the Boltzmann distribution:[25]

[4]

where R_{T0} is equal for all cells provided that they have similar geometrical dimensions. As expected, the slope of the semi-logarithmic plot resulted in being the same for all the investigated PEs.[29] A value of about 67 mV per decade was drawn, which is in good agreement with the theoretically predicted value of 58 mV per decade [25] at 293.15 K.

R_T values associated with different breeds of PEs were instead found to be significantly divergent; BB-based PEs were characterized by an overall R_T value that was remarkably lower than those corresponding both the linear NRs-based PEs (AR16, AR4, AR8) and their homologous B-NRs.

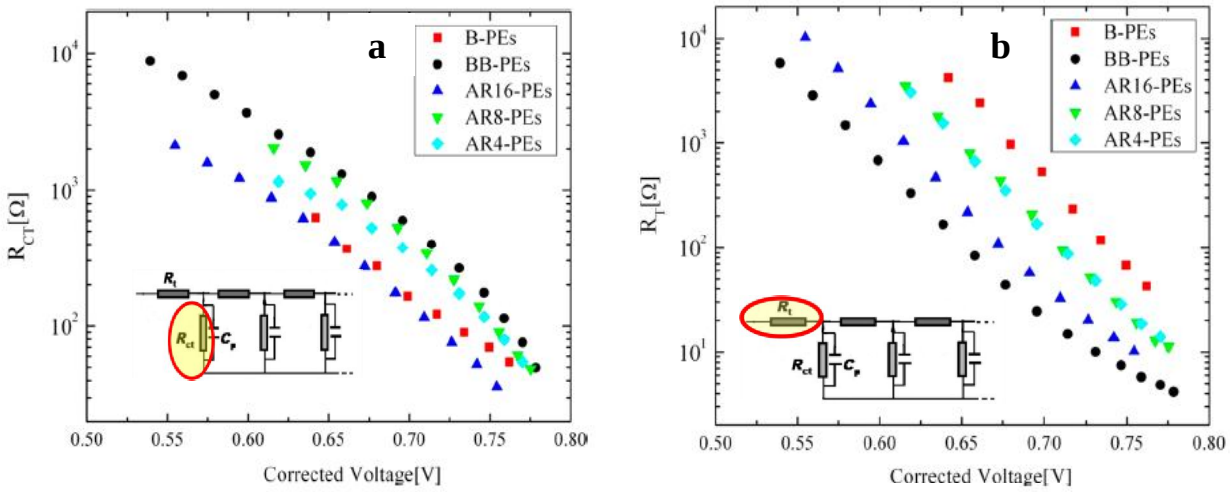

Figure 5. Charge-transfer resistance a) and transport resistance b) of the five different TiO_2NRs-based PEs as a function of the corrected bias voltage

At this point, it deserves recalling that the absolute values R_T and R_{CT} are of limited usefulness to the purpose of ranking the performances of different devices. For example, R_T and R_{CT} are both extensive parameters that scale with the overall TiO_2 surface area available and additionally depend on the actual number of grain boundaries and lattice defects in the films. As opposed, the R_{CT}/R_T ratio is a more reliable indicator of the genuine electron-collection efficiency of the devices.[30] The competition between the collection and the recombination of electrons can be thus expressed in terms of the electron diffusion length L_n. The latter is generally regarded as the most useful parameter to unambiguously compare the electron transport prerogatives of the photoelectrodes. Nevertheless, it is

worthy to emphasize that a rigorous determination of L_n should be performed under specific working conditions.[31]

Coherently with the aim of the present study, the EIS-derived extensive parameters were used to estimate L_n by adopting the quasi-static approximation model proposed by Bisquert et al:[32,33]

5 — [5]

where *d* is the film thickness.

The extrapolated values of L_n for every PE are plotted in Figure 6 as a function of the corrected voltage. As already reported in our previous work,[34] BB-NRs-based PEs revealed the highest average electron diffusion length, according to the order: BB-PEs > AR16-PEs > AR8-PEs > AR4-PEs 10 > B-PEs. This sequence suggested a corresponding meaningful hierarchy holding among the values of the photo-generated charge carrier collection efficiency. An electron diffusion length that is much larger than the film thickness should be expected to afford a quantitative collection of photo-generated charge carriers.

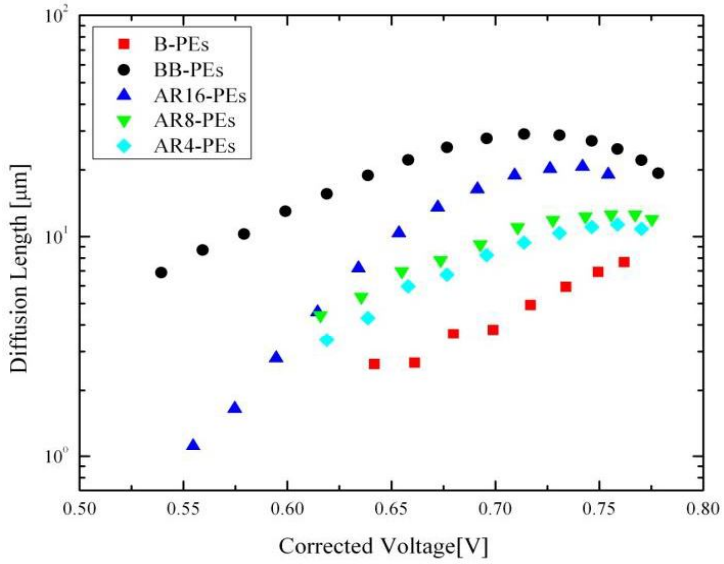

15 **Figure 6.** Diffusion length of the five different TiO_2NRs-based photoelectrodes as a function of the corrected bias voltage obtained from impedance spectra in the dark condition

From the here reported analysis an intrinsic correlation between the intimate structure of the NRs building blocks and the photovoltaic performances of the PEs was deduced and thereafter adopted to 20 maximize the performances of NRs-based DSCs through the implementation of engineered multilayered PEs which embody different breeds of NRs with synergistic peculiarities.

As first issue, several combinations of NRs and several PE thicknesses (from 3 um to 17 um) have been explored with the aim to get an effective balance among the above referred, often competing,

specific features of three nanomorphologies, namely AR4, AR16 and BB. A summary of the most elucidative tests has been reported in the Table II.

At relatively low thicknesses (e.g. 3 μm), AR4-based PEs showed the best performances, this being in good agreement with their superior dye-loading capability. As the thickness grew up to 7 μm, the photocurrent of PEs constituted by AR16-NRs overcame that one of the corresponding AR4-based film, despite their relatively lower surface area. These observations suggested us to exploit the possible synergistic effect of a suitable combination of AR4- and AR16-based films in the frame of a bi-layer architecture. Such structure actually demonstrated to be even more efficient than the corresponding monolayers: a 7 μm-thick PE composed of an AR4-based bottom layer (thickness 3 μm) and an AR16-based top layer (thickness 4 μm) indeed generated a short-circuit current density as high as 13.41 mA cm^{-2}, when compared with the values of 10.76 and 12.70 mA cm^{-2} which were measured in the case of 7 μm-thick AR4- and AR16-PEs, respectively.

Table II. Photovoltaic parameters of different NRs-based photoanodes recorded on sensitized 0.16 cm2 electrodes under 1 sun illumination (AM 1.5, 100 mW cm^{-2}); devices masked with 0.25 cm2 black tape

	η %	FF	Voc	Jsc
AR4: 3 μm	**4.46**	0.71	0.79	7.95
AR16: 3 μm	**4.15**	0.71	0.82	7.12
BB: 3 μm	**3.53**	0.73	0.84	5.75
AR4: 7 μm	**5.95**	0.70	0.79	10.76
AR16: 7 μm	**7.20**	0.70	0.81	12.70
BB: 7 μm	**5.44**	0.72	0.82	9.22
AR4 (3 um) + AR16 (4 um): 7 μm	**7.49**	0.69	0.81	13.41
AR4 (10 um)	**6.19**	0.68	0.77	11.82
AR16 (10 um)	**7.91**	0.67	0.79	14.95
BB (10 um)	**5.83**	0.71	0.81	10.14
AR4 (17 um)	**7.24**	0.69	0.76	13.82
AR16 (17 um)	**8.55**	0.68	0.78	16.12
BB (17 um)	**6.86**	0.70	0.80	12.25
ML-DSC 10 um (3 AR4 + 7 AR16)	**8,18**	0,69	0,81	14,64
ML-DSC 14 um (3 AR4 + 4 AR16 + 7 BB)	**9,40**	0,69	0,81	16,81
ML-DSC 15 um (3 AR4 + 7 AR16 + 5 BB)	**9,62**	0,69	0,80	17,43
ML-DSC 17 um (7 AR4 + 3 AR16 + 7 BB)	**9,20**	0,69	0,79	16,87

We then tested the performances of homogeneous PE at higher thicknesses and we could conclude that light absorption saturation for both AR14 and AR16 films reasonably occurs in the first 10-12 um-thick layer and that a considerable growth of the film thickness up to 17 didn't really turn into a beneficial effect on the performances: at thickness higher than 12 μm the competition between the collection and the recombination of electrons becomes disadvantageous, in particular for AR4-NRs. Moreover, some issues concerning the quality of so high films should be also addressed: extremely small nanorods as those ones referred in this work tend to form severe cracks during the sintering process at thicknesses higher than 12-14 um.

On the other side, they highly transparent even at relatively high thickness (see Figure 4a) due to the homogeneous assembly of their extremely small building blocks, which prevented any light-scattering phenomena in the visible spectrum. This implies on the other side that a further enhancement of the photovoltaic performances may be achievable through the introduction of a suitable photon- recycling structure. PEs based on BB-NRs instead, due to their relatively bigger size, were found to work as light-scattering centres while maintaining good dye loading capability and allowing a surprisingly high photocurrent density (9.22 mA cm^{-2} for 7 μm-thick PEs). These photoanodes were indeed characterized by the longest value of the electron diffusion length (see Figure 6), which is almost two times higher than AR16-PE and three times higher than AR4-PEs. They also offered the most favourable conditions to minimize the charge recombination at the interface with electrolyte, as attested by their higher open-circuit voltage (0.82 V). This bheaviour could be ascribed to the particular bundle-like architecture concerned with their monocrystalline nature, where the individual rod-shaped arms were assembled so as to guarantee crystal lattice continuity at the relevant branch points and, hence, to dramatically reduce the density of electron trap states at surfaces and grain boundaries. [35]

We thus exploited all these findings to design an engineered PE which embodied the above referred three families of shape-tailored TiO_2 nanocrystals within a unique multistack architecture in such a way to complementarily and synergistically exploit the properties associated with their specific topological features. A cross section SEM image of such nanostructured film is reported in Figure 8.

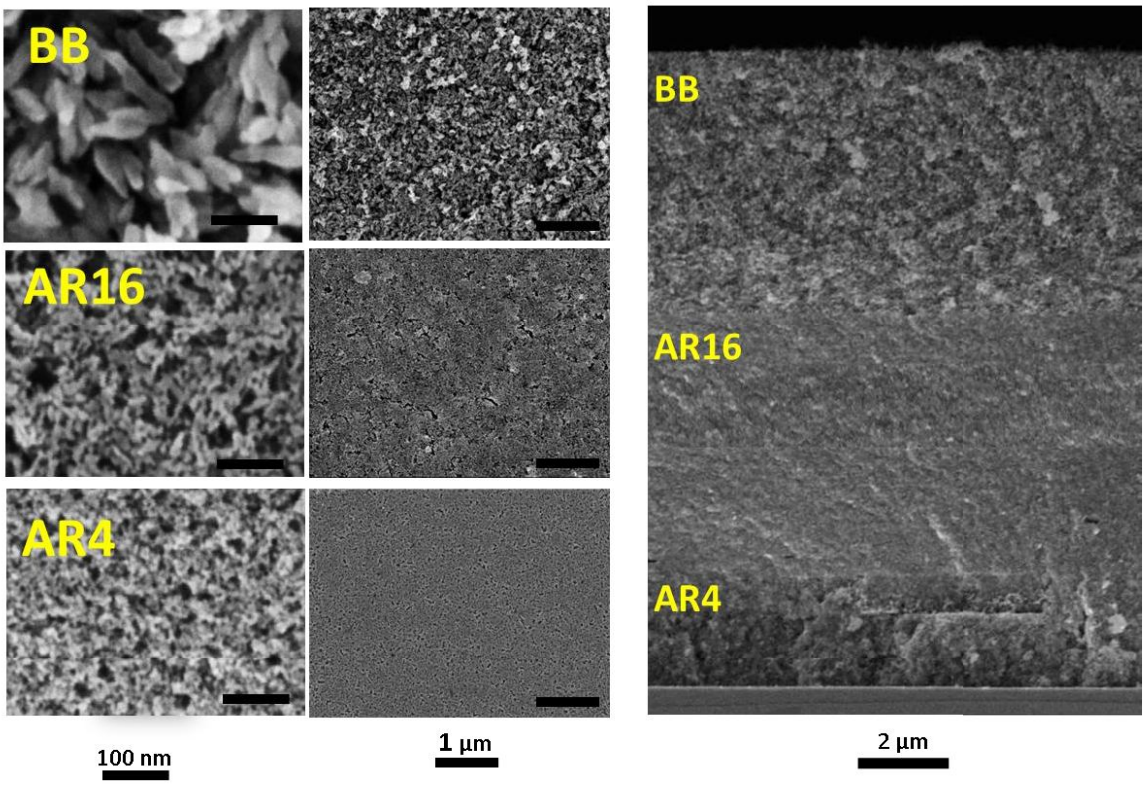

Figure 7 Cross sectional SEM view of the engineered three-stack photoelectrode.

An as high PCE as 10.26% was achieved with a 17 µm thick photoanode (ML-DSC) which incorporated a bottom layer (3 µm) made of AR4-NRSs, a middle layer (7 µm) made of AR16-NRs and a top layer (7 µm) made of hyperbranched BB. The resulting photovoltaic parameters are summarized in Table III and J-V curves are shown in Figure 8a. ML-DSC were distinguished by a J_{SC} of 18.10 mA cm^{-2}, an open-circuit voltage (V_{OC}) of 0.81 V and a fill factor (FF) of 0.70, while a standard double-layer nanoparticles-based photoanode (D-DSC) with the same thickness gave a PCE of only 8.21% and J_{SC} of 15.06 mA cm^{-2}. Our PEs thus attained an improvement of almost 25% with respect with the efficiency afforded by reference photoelectrode. The deposition of a BB-based layer on the top of the AR4+AR16 PE has been revealed in fact to be the most suitable approach to generate effective light scattering without detrimentally sacrificing any other desirable properties, as well as the surface area and electron transport. It has to be remarked also that N719 with a commercial degree of purification was used in all the experiments.

Table III. Photovoltaic parameters of DSCs based on multilayered NRs and Dyesol-based photoelectrodes recorded on sensitized 0.16 cm2 electrodes under 1 sun illumination (AM 1.5, 100 mW cm^{-2}); devices masked with 0.25 cm2 black tape

Device	η%	FF	V_{OC} (V)	J_{SC} (mA cm^{-2})	Dye loading (mol cm^{-2}) x 10^{-7}
ML-DSC 17 µm (3 AR4 + 7 AR16 + 7 BB)	10.26	0.70	0.81	18.10	2.68
D-DSC 17 µm (12 18NR-T + 5 18NR-AO)	8.21	0.69	0.79	15.06	1.97

The increased efficiency of our ML-DSC was primarily due to the enhancement in J_{SC} that could be partially related to the larger total number of dye molecules adsorbed onto the electrode ($2.68x10^{-7}$ mol*cm^{-2}), being higher than the reference nanoparticles-based electrode ($1.97x10^{-7}$ mol*cm^{-2}) , but also the significant improvement of the charge collection efficiency guaranteed by the fine calibration of the three layers features.

Finally, the reproducibility of the photovoltaic performance was tested by processing 11 PEs for both the kind of optimized cells. The distribution of η is shown in Figure 8b.

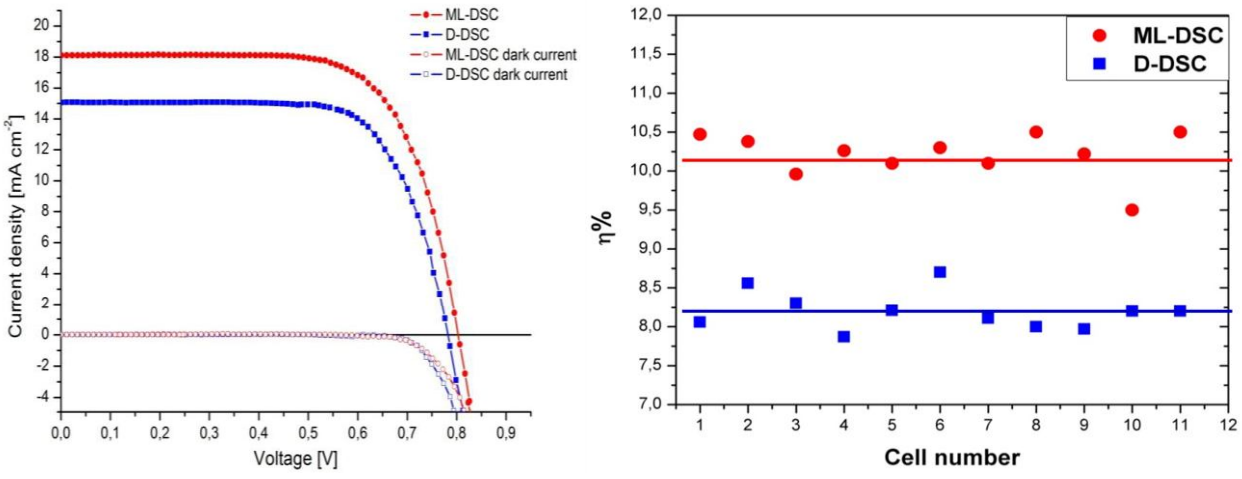

Figure 8. a) IV curves of the best cells and b) reproducibility of photovoltaic parameters of DSCs based on multilayered photoanodes and on commercial nanocrystals under 1 sun illumination (AM 1.5, 100 mW cm^{-2}). PV Characteristics recorded on sensitized 0.16 cm2 electrodes; devices masked with 0.25 cm2 black tape.

CONCLUSIONS

It has been ascertained that DSCs based on high aspect-ratio linear nanorods allow for a remarkable improvement in the charge-collection efficiency due to minimization of detrimental charge-recombination processes at the photoelectrode/electrolyte interface. On the other side, DSCs fabricated from branched nanocrystals with a peculiar bundle-like configuration are characterized by a drastic reduction of undesired charge-trapping phenomena. These findings have been thus advantageously exploited in the design and fabrication of an an innovative photoelectrode's architecture which embodies three TiO_2 layers with different –basically complementary and synergistic- peculiarities: a bottom layer, made by small nanorods which assure tremendous specific surface area and exceptional transparency in the dye's absorption spectrum; a middle layer made by high aspect-ratio nanorods which guarantee a superior electron transport and good dye loading capability; a third upper layer made of relatively bigger hyperbranched nanocrystals which offer adequate light scattering capacity and favorable interfacial charge-transfer characteristics. An as high power conversion efficiency as 10.26% was eventually achieved by means of our best multilayer configuration.

AKNOWLEDGMENTS

This work has been partially supported by the European project ESCORT - Efficient Solar Cells based on Organic and hybrid Technology (7th FWP—reference number 261920) and by the national project MAAT (MIUR – PON02_00563_3316357 – CUP B31C12001230005). The authors thank Davide P. Cozzoli and Maria Belviso for the precious technical support and Filippo De Angelis for helpful discussions. Daunia Solar Cells is also gratefully acknowledged for funding some correlated activities on dye solar cells.

REFERENCES

[1] A. Hagfeldt, G. Boschloo, L. Sun, L. Kloo, H. Pettersson, Chem. Rev. 110 (2010) 6595.
[2] Q. Zhang, G. Cao, Nano Today 6 (2011) 91.
[3] M. Manca, F. Malara, L. Martiradonna, L. De Marco, R. Giannuzzi, R. Cingolani, G. Gigli, Thin Solid Films, 23 (2010) 7147.
[4] J. Van de Lagemaat, A. J. Frank, J. Phys. Chem. B 104 (2000) 4292.
[5] J. Bisquert, V. S. Vikhrenko, J. Phys. Chem. B 108 (2004) 2313.
[6] M. Law, L.E. Greene, J.C. Johnson, R. Saykally, P.D. Yang, Nature Mater. 4 (2005) 455.

[7] S.Y. Huang, G. Schlichthorl, A.J. Nozik, M. Grätzel, A.J. Frank, J. Phys. Chem. B 101 (1997) 2576.
[8] J. Van de Lagemaat, N. Park, A. Frank, J. Phys. Chem. B 104 (2000) 2044.
[9] A. Yella, H. W. Lee, H. N. Tsao, C. Yi, A. K. Chandiran, M. K. Nazeeruddin, E. W. G. Diau, C. Y. Yeh, S. M. Zakeeruddin, M. Grätzel, Science, 334 (2011), 629.
[10] J. Jiu, S. Isoda, F. Wang, M. Adachi, J. Phys. Chem. B 110 (2006) 2087.
[11] S. H. Kang, S. H. Choi, M. S. Kang, J. Y. Kim, H. S. Kim, T. Hyeon, Y. E. Sung, Adv. Mater. 20 (2008) 54.
[12] S. Lee, I. S. Cho, J. H. Lee, D. H. Kim, D. W. Kim, J. Y. Kim, H. Shin, J. K. Lee, H. S. Jung, N. G. Park, K. Kim, M. J. Ko, K. S. Hong, Chem. Mater. 22 (2010) 1958.
[13] L. De Marco, M. Manca, R. Giannuzzi, F. Malara, G. Melcarne, G. Ciccarella, I. Zama, R. Cingolani, G. Gigli, J. Phys. Chem. C 114 (2010) 4228.
[14] Y. Qiu, W. Chen, S. Yang, Angew. Chem. Int. Ed. 49 (2010) 3675.
[15] J. K. Oh, J. K. Lee, H. S. Kim, S. B. Han, K.W. Park, Chem. Mater. 22 (2010) 1114.
[16] B. Koo, J. Park, Y. Kim, S. H. Choi, Y. E. Sung, T. Hyeon, J. Phys. Chem. B, 110 (2006) 24318.
[17] R. Buonsanti, E. Carlino, C. Giannini, D. Altamura, L. De Marco, R. Giannuzzi, M. Manca, G. Gigli, P. D. Cozzoli, J. Am. Chem. Soc. 133 (2011) 19216.
[18] X. Feng, K. Zhu, A. J. Frank, C. A. Grimes, T. E. Mallouk, Angew. Chem. Int. Ed. 51 (2012) 2727.
[19] X. Feng, K. Shankar, O. K. Varghese, M. Paulose, T. J. Latempa, C. A. Grimes, Nano Lett. 8 (2008) 3781.
[20] Q. Zheng, H. Kang, J. Yun, J. Lee, J. H. Park, S. Baik, ACS Nano, 5 (2011) 5088.
[21] M. Ye, X. Xin, C. Lin, Z. Lin, Nano Lett. 11 (2011) 3214.
[22] L. De Caro, E. Carlino, G. Caputo, P. D. Cozzoli and C. Giannini, Nat. Nanotechnol., 5 (2010) 360.
[23] P. D. Cozzoli, A. Kornowski and H. Weller, J. Am. Chem. Soc., 125 (2003) 14539.
[24] J. Joo, S. G. Kwon, T. Yu, M. Cho, J. Lee, J. Yoon and T. Hyeon, J. Phys. Chem. B, 109 (2005) 15297.
tzel, F. Fabregat-Santiago, I. Mora-Sero, J. Bisquert, T. Bessho, H. Imai, J. Phys. Chem. B 110 (2006) 25210.
[26] F. Fabregat-Santiago, J. Bisquert
tzel, J. Phys. Chem. C, 111 (2007) 6550.
[27] J. Bisquert, I. Mora-Sero, J. Phys. Chem. Lett. 1, (2010) 450.
[28] J. Villanueva-Cab, H. Wang, G. Oskam, L. Peter, J. Phys. Chem. Lett. 1, (2010) 748.
[29] F. Fabregat-Santiago, J. Bisquert, G. Garcia-Belmonte, G. Boschloo, A. Hagfeldt, Sol. Energy Mater. Sol. Cells 87, (2005) 117.
[30] T. Hoshikawa, M. Yamada, R. Kikuchi, K. Eguchi, J. Electrochem. Soc. 152 (2005) E68.
[31] P. R. F.Barnes, B. O'Regan, J. Phys. Chem. C, 114 (2010) 19134.
[32] F. Fabregat-Santiago, G. Garcia-Belmonte, I. Mora-Sero, J. Bisquert, Phys. Chem. Chem. Phys, 13 (2011) 9083.
- - - , J. Phys. Chem. C, 113 (2009) 17278.
[34] L. De Marco, M. Manca, R. Buonsanti, R. Giannuzzi, F. Malara, P. Pareo, L. Martinadonna, N. M. Giancaspro, P. D. Cozzoli, G. Gigli, J. Mater. Chem., 21 (2011) 13371.
[35] R. Agosta, R. Giannuzzi, L. De Marco, M. Manca, M. R. Belviso, P. D. Cozzoli, G. Gigli, J. Phys. Chem. C 117 (2013) 2574.